LBNL FORGE Project 3-2535 Task 3 Milestone Report 3

Development of a Reservoir Seismic Velocity Model and Seismic Resolution Study

Roland Gritto, Array Information Technology, Berkeley, CA

Don Vasco, Earth and Environmental Sciences, Lawrence Berkeley National Laboratory, Berkeley, CA

Coral Chen, University of California, Berkeley, CA

1. Introduction

In FORGE project 3-2535, Array Information Technology (AIT) and Lawrence Berkeley National Lab (LBNL) developed a representative 3D seismic velocity model in support of future research activities. Seismic velocities for the 3D model were taken from seismic reflection profiling and available well logs, obtained during prior FORGE phases. As such, the model was developed using a combination of measurements and datasets. Modeling seismic wave propagation associated with the seismicity recorded during Phase III of the April 2022 FORGE stimulation in well 16A-32 was conducted to investigate the dependence of the resolution of the seismic waves in the stimulated volume on the geometry of seismic and DAS sensor arrays. The goal was to investigate usage of the available data sets from different sensors to indicate which data and/or combinations of datasets yield the optimum seismic resolution in the targeted fracture volume. The results indicate whether future seismic imaging campaigns will be able to reliably image the stimulated reservoir volume. Additionally, the outcome can be used to optimize the number and the experimental geometry for the placement of seismic sensors during the upcoming stimulation in well 16B-32. In the following, we will describe the development of the velocity model and report the results of our seismic resolution analysis.

2. Development of a Reservoir Seismic Velocity Model (Task 3.1)

During the exploration phase of the FORGE site in Milford, UT, a seismic reflection survey was conducted to image the subsurface geology, including the sedimentary overburden and the granitic basement (Miller, 2019). The reflection survey consisted of 986 vibroseis source locations and 1,740 geophone receivers. The geometry of the survey is shown in Figure 1, where the source and geophone positions are given by the open black circles and black dots, respectively. The development of the initial velocity model was based on RMS velocities of the reflection survey, which were scaled to match the observed velocities obtained by seismic logging in the shallow sedimentary section and in the underlaying basement rock. The velocities in the sedimentary layers were derived from a vertical seismic profiling (VSP) survey recorded by a distributed acoustic sensing (DAS) string, while the velocities in the basement were obtained by sonic logging in well 78B-32. The velocity profile of the initial model, scaled to the shallow and deep velocity logs, is presented in Figure 2. After scaling, the initial model fits the logging velocities quite well.

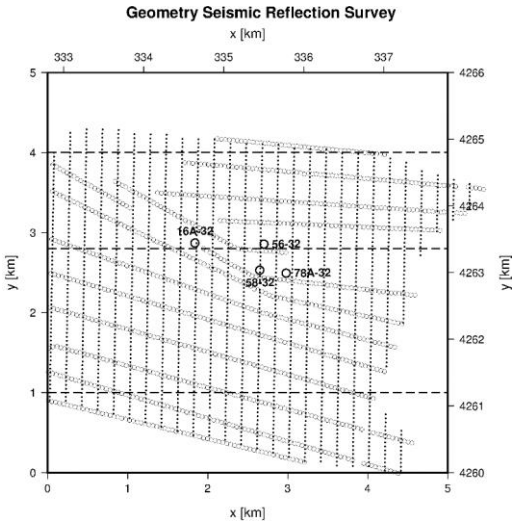

Figure 1. Map of the FORGE area with the geometry of the seismic reflection survey. The vibroseis source locations and geophone positions are given, respectively, by the open black circles and black dots. A subset of FORGE wells are shown for reference. The dashed lines at y = 1.0 km, 2.8 km, and 4.0 km denote the locations of vertical velocity profiles shown hereafter.

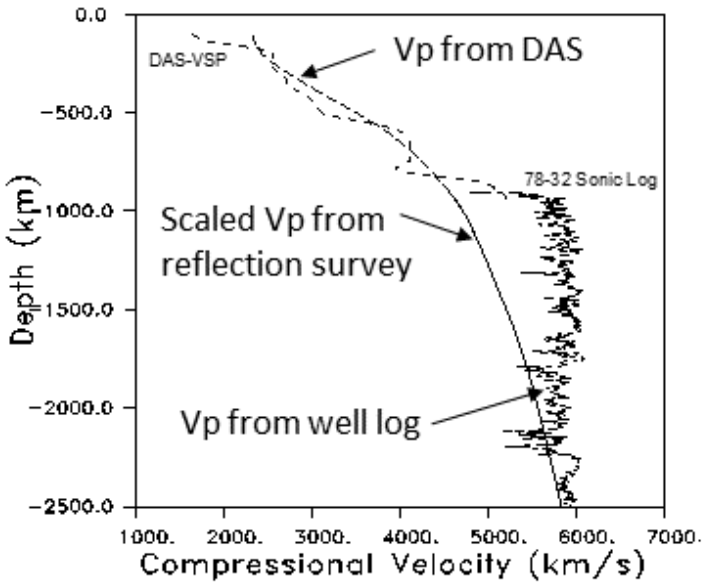

Figure 2. Profiles of the P-wave velocities derived from the reflection survey, the VSP experiment recorded by DAS, and the sonic logging in well 78B-32. The velocity profile from the reflection survey was scaled by a factor of 1.4 to match velocities observed in the boreholes.

Three vertical cross sections of the initial velocity model obtained from the seismic reflection survey are shown in Figure 3. The sediments, represented by P-wave velocities from 3.0 km/s to 4.5 km/s, are dipping slightly to the West. The basement interface is represented by a velocity increase to 5 km/s at a depth of approximately 1 km. In this model, basement velocities are increasing from 5 km/s to 6 km/s at depth, with the FORGE reservoir located within rocks in the upper 5km/s range.

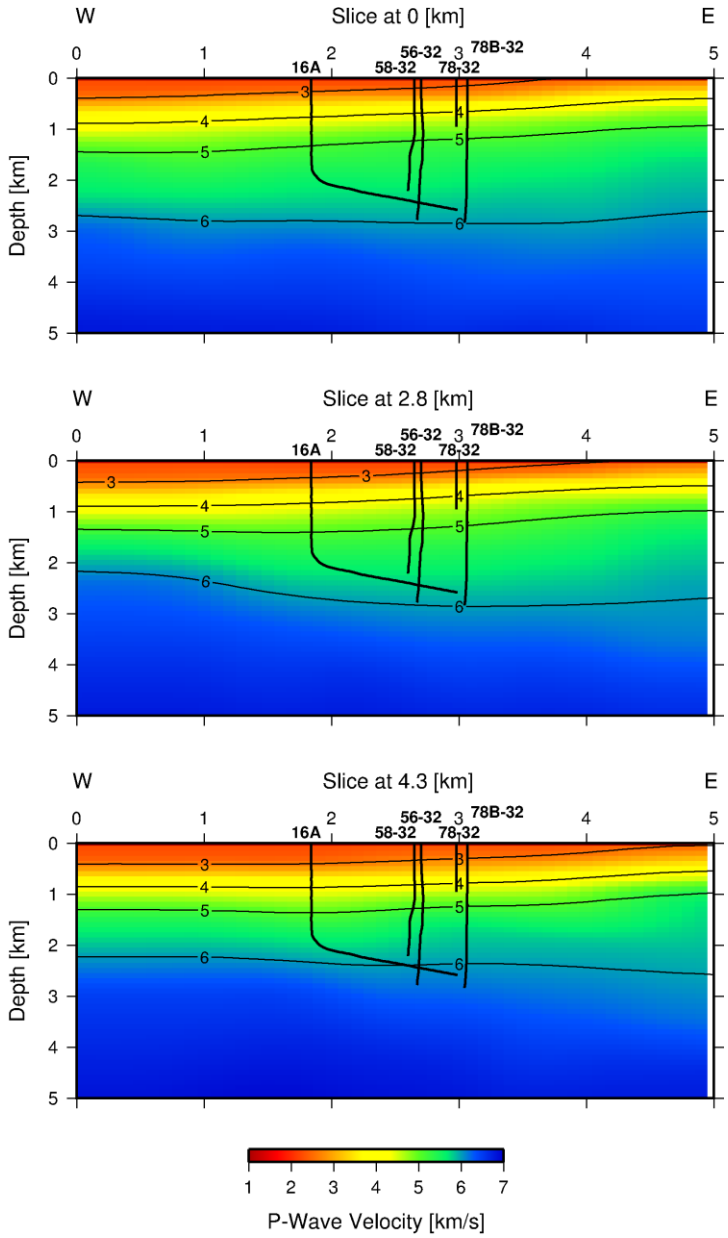

Figure 3. East-west cross section through the 3D P-wave starting velocity model obtained from scaled RMS velocities of the seismic reflection survey. The location of each cross section is noted at the top of the panels and refers to the profiles denoted by the dashed lines in Figure 1. The wells are shown for reference.

A section of the seismic reflection survey is presented in Figure 4. It shows an east-west cross section through the center of the FORGE site. The basement interface is characterized by a strong reflection dipping from east to west, which is recovered in the velocity model in Figure 3. The dip of the interface in both figures is different due to the difference in vertical scale.

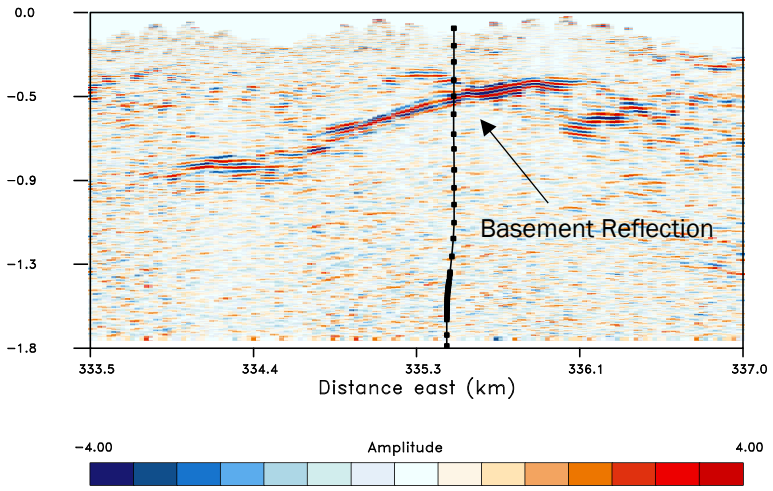

Figure 4. Cross section of seismic reflection survey through the center of the FORGE site with the basement interface denoted by the strong reflection event.

Because the velocities of the reflection survey are less reliable in the shallow sediments, and logs are not available for the shallow subsurface, it was decided to estimate the arrival times of the direct P-waves from the reflection data and inverting these data to obtain P-wave velocities. The direct P-waves are well suited to estimate the velocity in the shallow subsurface because they refract off the basement interface and mainly propagate in the sedimentary layer. Data processing was based on the software package PhaseNet (Zhu and Beroza, 2019), a deep-neural-network-based seismic arrival time picking method. PhaseNet uses seismic waveform data as input and generates probability distributions of seismic arrival times. The maxima in the probability distributions provide accurate arrival times for the seismic waves. The initial velocity model in Figure 3 was used to compute time windows on the waveforms for PhaseNet to estimate the arrival times of the direct P-wave for a subset of sources (Gritto et al., 2023). The travel times were subsequently inverted using an eikonal solver to update the initial velocity model.

The results, presented by Gritto et al. (2023), suggested that the velocities of the shallow sediments in the initial model (Figure 3) are too high, which may have resulted from scaling the RMS velocities to match the logging velocities in the initial stage of the model building. It is known that estimates of velocities derived from logging measurements tend to be higher than those from surface experiments, due to differences in scale of the seismic wavelengths of these techniques.

Therefore, we developed a new 3D velocity model, based on an initial model with slower sedimentary velocities and a slightly lower, constant basement velocity of 5.83 km/s, which was

used by Geo-Energie Suisse AG (GES) to analyze the seismicity observed during the Stage III stimulation in April 2022 (Pankow, 2022). This slower velocity model improved estimating the P-wave arrival times on the seismic waveform data, because the calculated time windows for the application of PhaseNet became more accurate. The new starting model is shown in Figure 5. The vertical scale of the model is limited to 3 km depth to better display the area of the proposed EGS reservoir. In comparison to the previous starting model in Figure 3, the lower sedimentary and basement velocities are visible.

For the development of the final P-wave velocity model, the complete dataset of seismic waveforms based on 986 source- and 1,740 receiver positions was processed, which resulted in more than 1,200,000 P-wave travel times. Computational node spacing was set to 125 m in horizontal and vertical direction. Vertical cross sections through the final P-wave velocity model are presented in Figure 6, which shows the model along the same profiles as before. The final model reveals a sedimentary structure with more heterogeneous velocities compared to the layered starting model. This is expected, as the starting model was based on RMS P-wave velocities from the seismic reflection data, which are estimated on the assumption of a layered medium.

The estimates of the final 3D velocity model are updated only in the sedimentary layers and along the top of the basement because the direct P-waves propagate mainly in the low velocity sediments and refract along the interface between the sediments and the fast-velocity basement. This is shown in Figure 7 for the profile at y = 2.8 km crossing through the FORGE site (ref. Figure 1). The figure shows the final velocity model and the P-wave rays paths for three representative source locations. For short source-receiver distances the rays turn and stay within the sediments which exhibit strong velocity gradients, while for longer source-receiver distances, the rays refract along the top of the basement. Therefore, the travel time inversion updates the velocities only in the sediments and in the top section of the basement.

A map view of horizontal sections through the final P-wave velocity model in the study area is presented in Figure 8. The sections cover the same area shown in Figure 1. While low-velocities of the sediments are observed throughout the study area (z = 0.125 km), the westward dip of the high-velocity basement becomes apparent with increasing depth of the sections. However, the contact between the sediments and the basement is not planar at intermediate depth (1.0 km, 1.5 km), which is indicated by the undulating contour lines of the velocity in north-south direction.

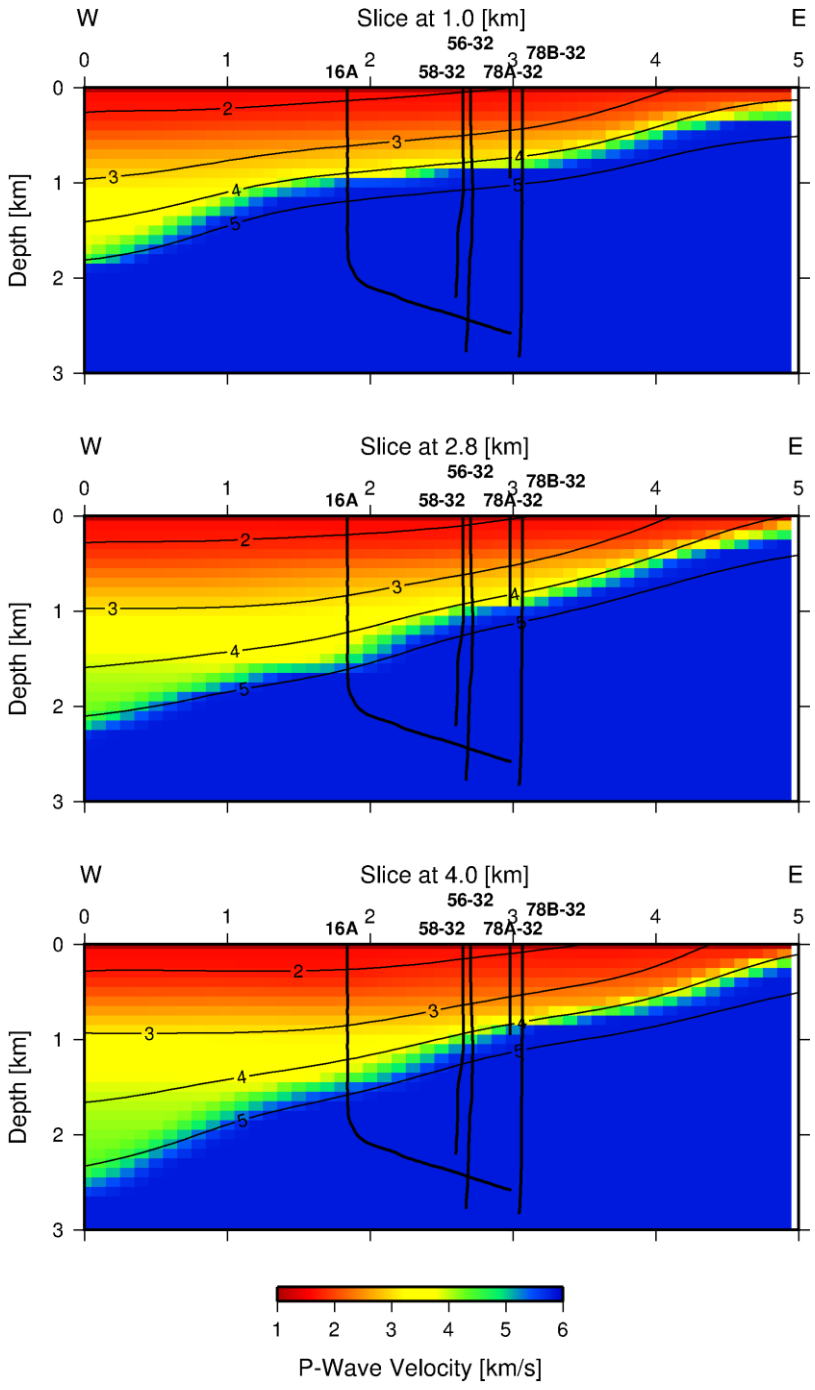

Figure 5. East-west cross section through the updated 3D P-wave starting velocity model. The location of each cross section is noted at the top of the panels and refers to the profiles denoted by the dashed lines in Figure 1. The wells are shown for reference.

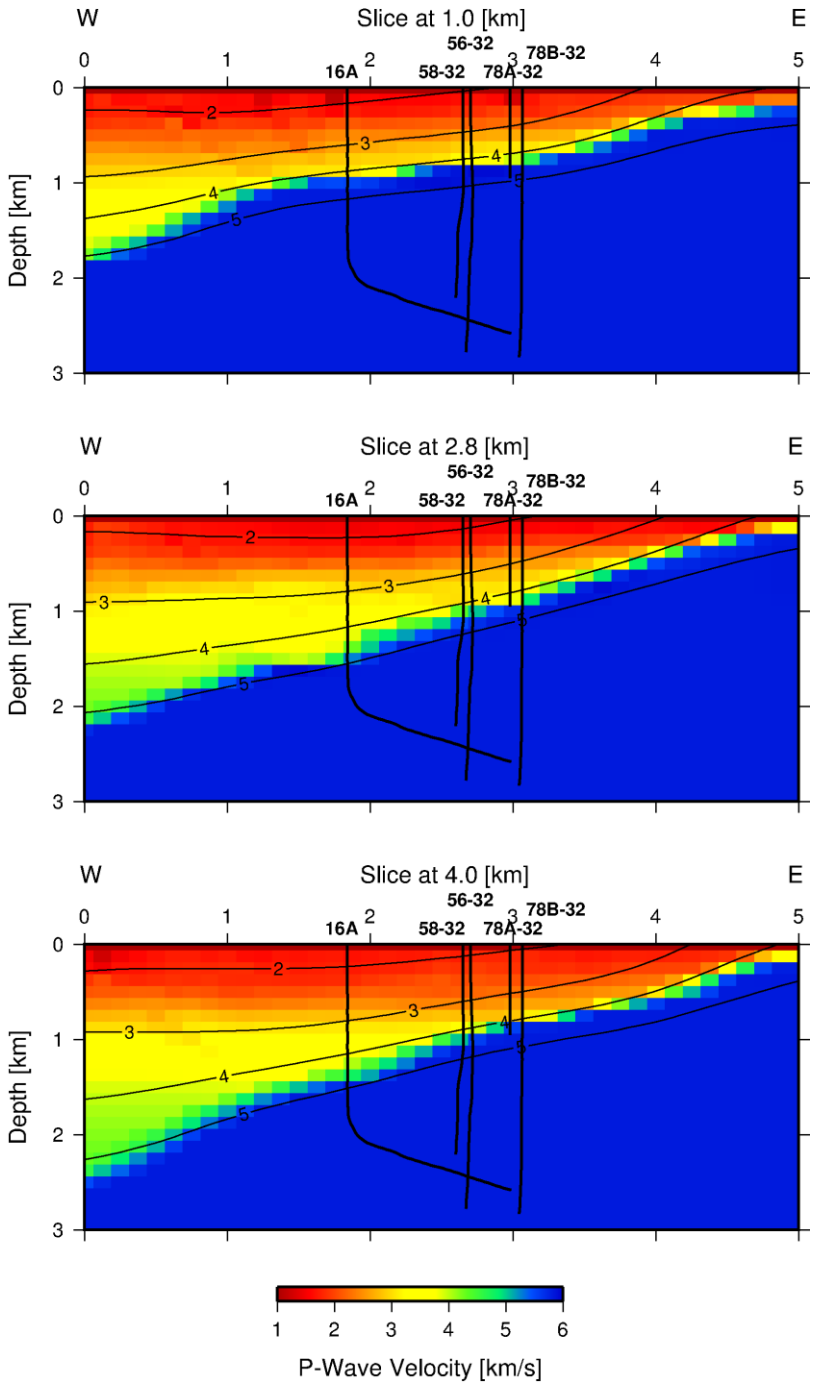

Figure 6. East-west cross section through the 3D P-wave final velocity model. The location of each cross section is noted at the top of the panels and refers to the profiles denoted by the dashed lines in Figure 1. The wells are shown for reference.

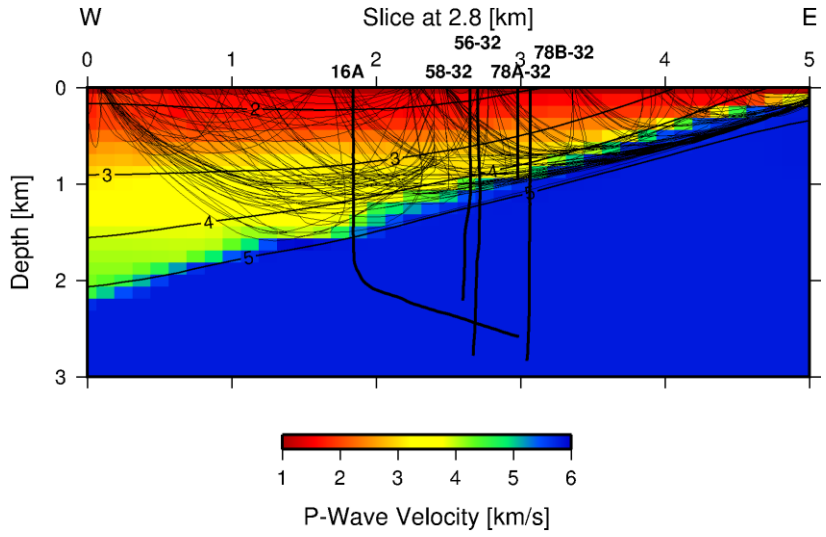

Figure 7. East-west cross section through the 3D P-wave final velocity model for the cross section traversing the FORGE site. The raypaths of the P-waves are shown for three representative source locations. The wells are shown for reference.

A detailed view of the perturbations between the final and the starting P-wave velocity model (final -minus- starting model) is presented in Figures 9 and 10. The figures show the regions in the model where the inversion had sufficient resolution to update the starting velocity model. At shallow depth and in the center of the study area, the final model reveals lower sedimentary P-wave velocities than the starting model. However, along the margins of the study area and at greater depth in the western parts, the final model reveals higher velocities than the starting model.

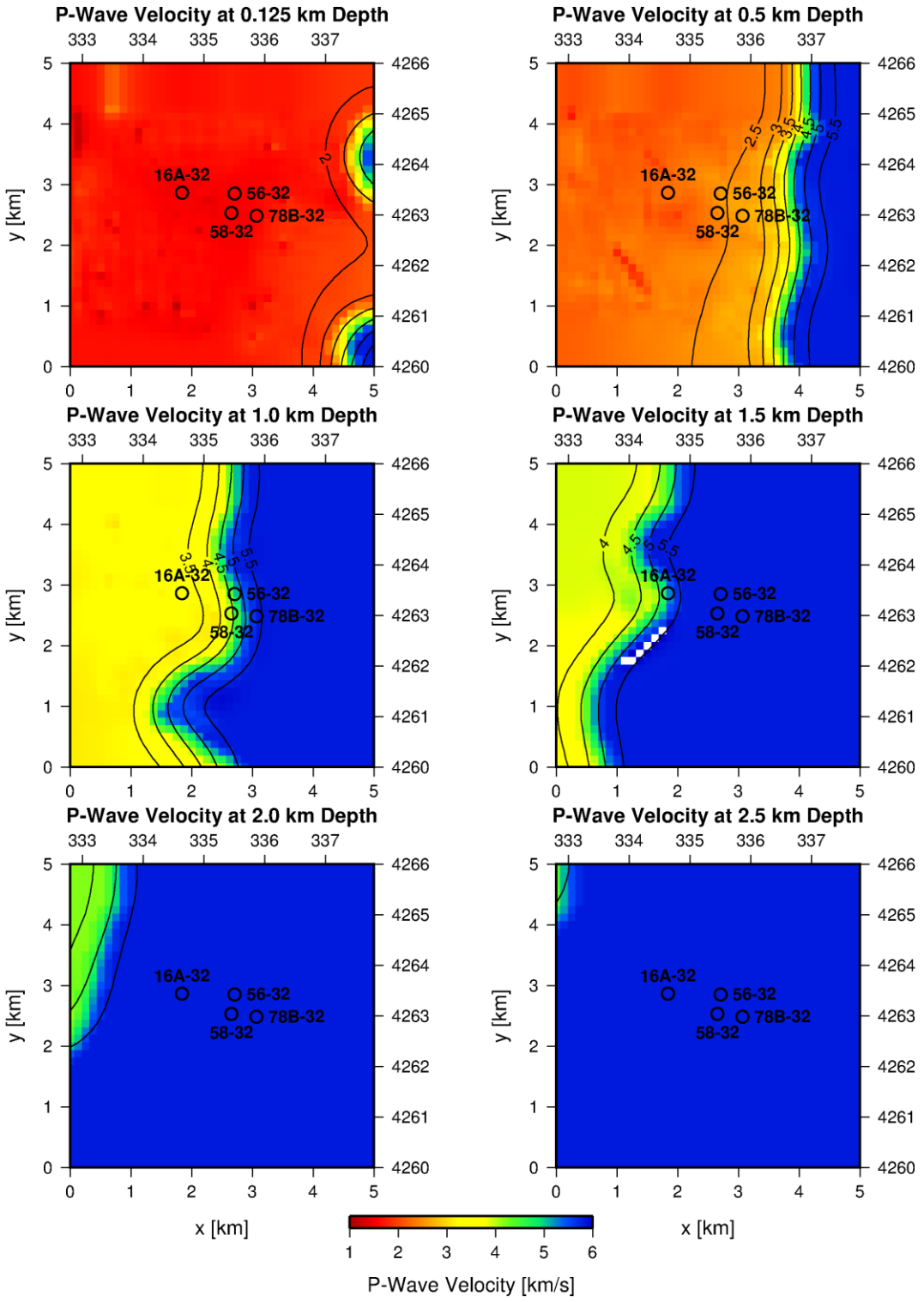

Figure 8. Horizontal sections through the 3D P-wave final velocity model. The depth is noted at the top of each panel. The locations of the wells are shown for reference.

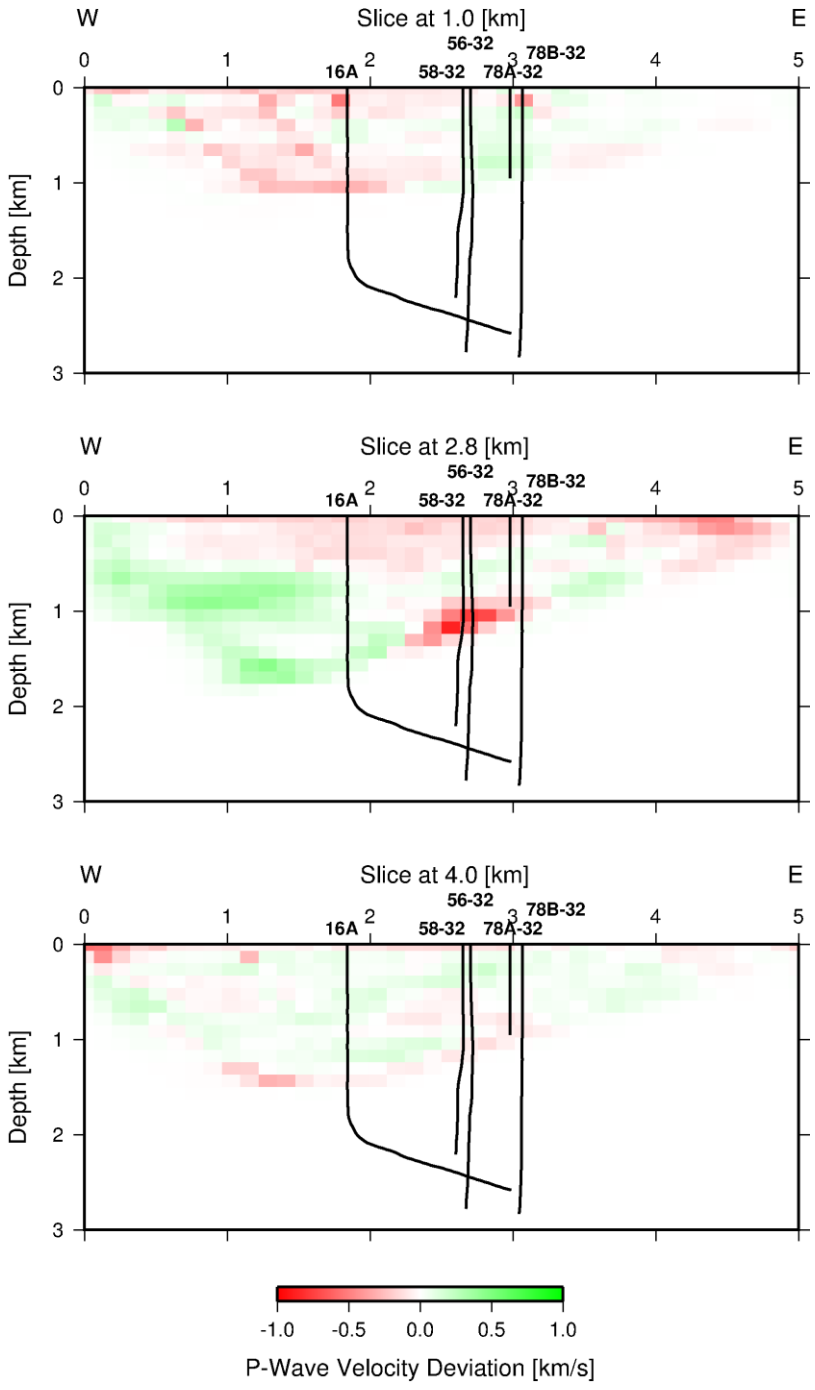

Figure 9. East-west cross section with differences between the starting and final 3D P-wave velocity model. The location of each cross section is noted at the top of the panels and refers to the profiles denoted by the dashed lines in Figure 1. The wells are shown for reference.

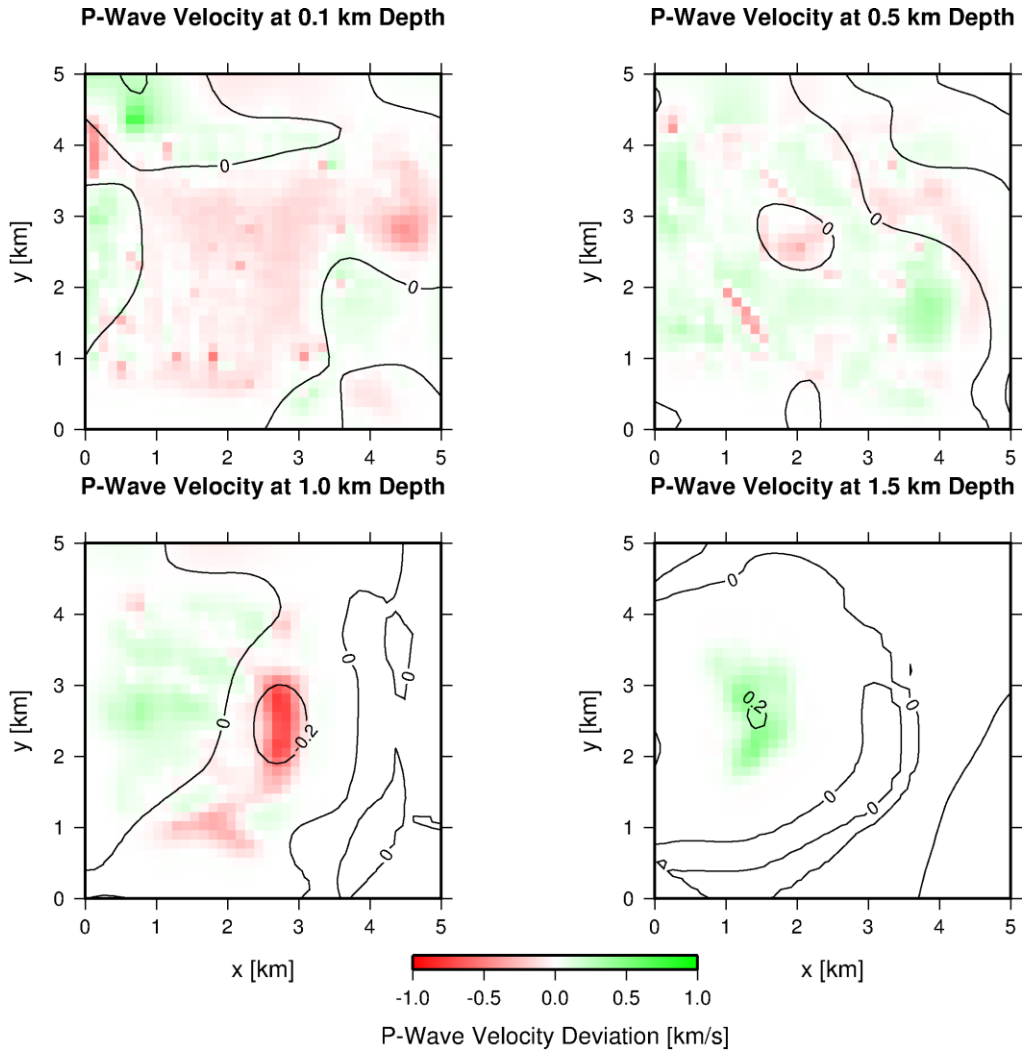

Figure 10. Horizontal sections with differences between the starting and final 3D P-wave velocity model. The depth is noted at the top of each panel. Only the depth with sufficient resolution are shown. The locations of the wells are shown for reference.

The analysis of the seismic reflection data yielded travel times for the direct propagating P-waves only because the seismic sources consisted of vibroseis trucks that generate P-waves only. While S-waves are generated by conversion of the P-waves in the subsurface, their amplitudes are low and suffer from low-signal-to-noise amplitude ratio as they are covered by larger amplitudes of P-wave coda. Therefore, an appropriate 3D S-wave model was developed using the ratio of Vp and Vs waves, which were obtained from the analysis of distributed acoustic sensing (DAS) data at the FORGE site (Lellouch et al., 2020). The DAS data were recorded in well 78A-32 with a gauge length of 10 m from 100 m to 950 m depth. Data from several perforation shots in well 58-32 were recorded by the DAS array and analyzed for P- and S-wave travel times (Lellouch et al., 2020). The resulting P- and S-wave velocity profiles are shown in Figure 11. For the current task, the P- and S-wave velocities were used to compute the Vp/Vs ratio over the same depth range (Figure

11). The Vp/Vs ratio was subsequently used to convert the 3D P-wave velocities in the sediments to 3D S-wave velocities. The DAS data were selected for this conversion as they offer the highest fidelity and resolution of S-wave velocities in the sediments. For the basement, an S-wave velocity of 3.41 km/s was chosen, which was used by Geo-Energie Suisse AG (GES) to analyze the seismicity observed during the Stage III stimulation in April 2022 (Pankow, 2022).

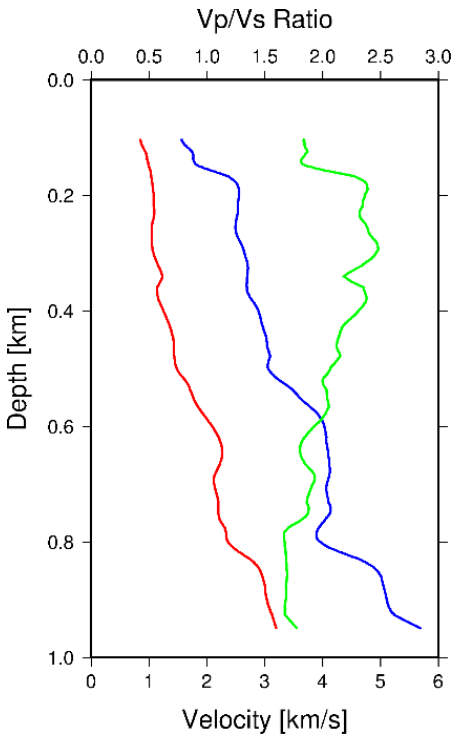

Figure 11. Profiles of P-wave velocity (blue), S-wave (red) velocity, and Vp/Vs ratio (green) as determined by DAS measurements in borehole 78A-32.

The resulting 3D S-wave velocity model is presented in Figures 12 and 13. As before, the borehole trajectories and well head locations are shown for reference. In the vertical (Figure 12) and horizontal sections (Figure 13) the sediments are characterized by low shear wave velocities (Vs = 0.5 km/s) in the near surface, which gradually increase to Vs = 2.0 km/s towards the basement interface. Similar to the P-wave velocities, the S-wave velocities in the basement remain constant at Vs = 3.41 km/s.

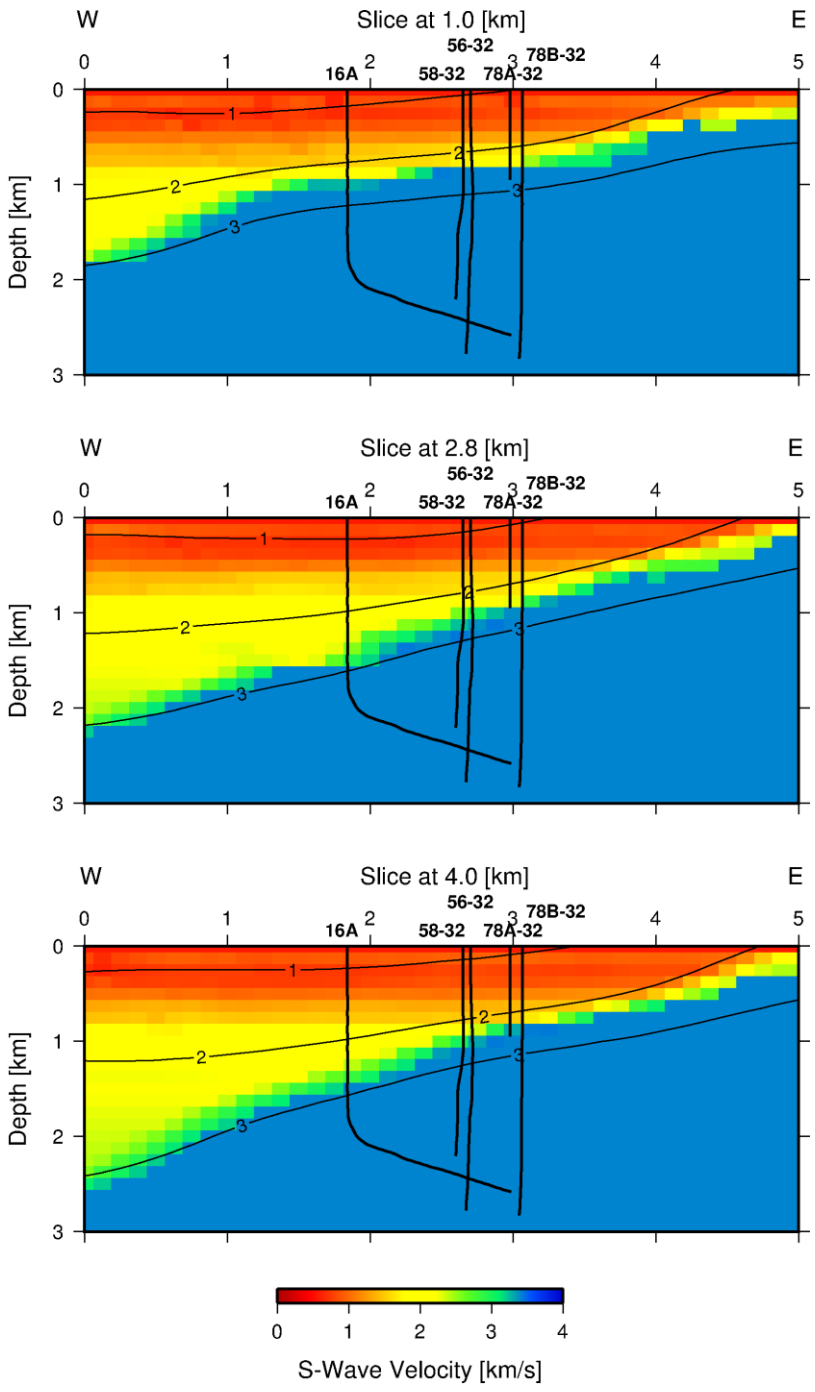

Figure 12. East-west cross section through the 3D S-wave velocity model. The location of each cross section is noted at the top of the panels and refers to the profiles denoted by the dashed lines in Figure 1. The wells are shown for reference.

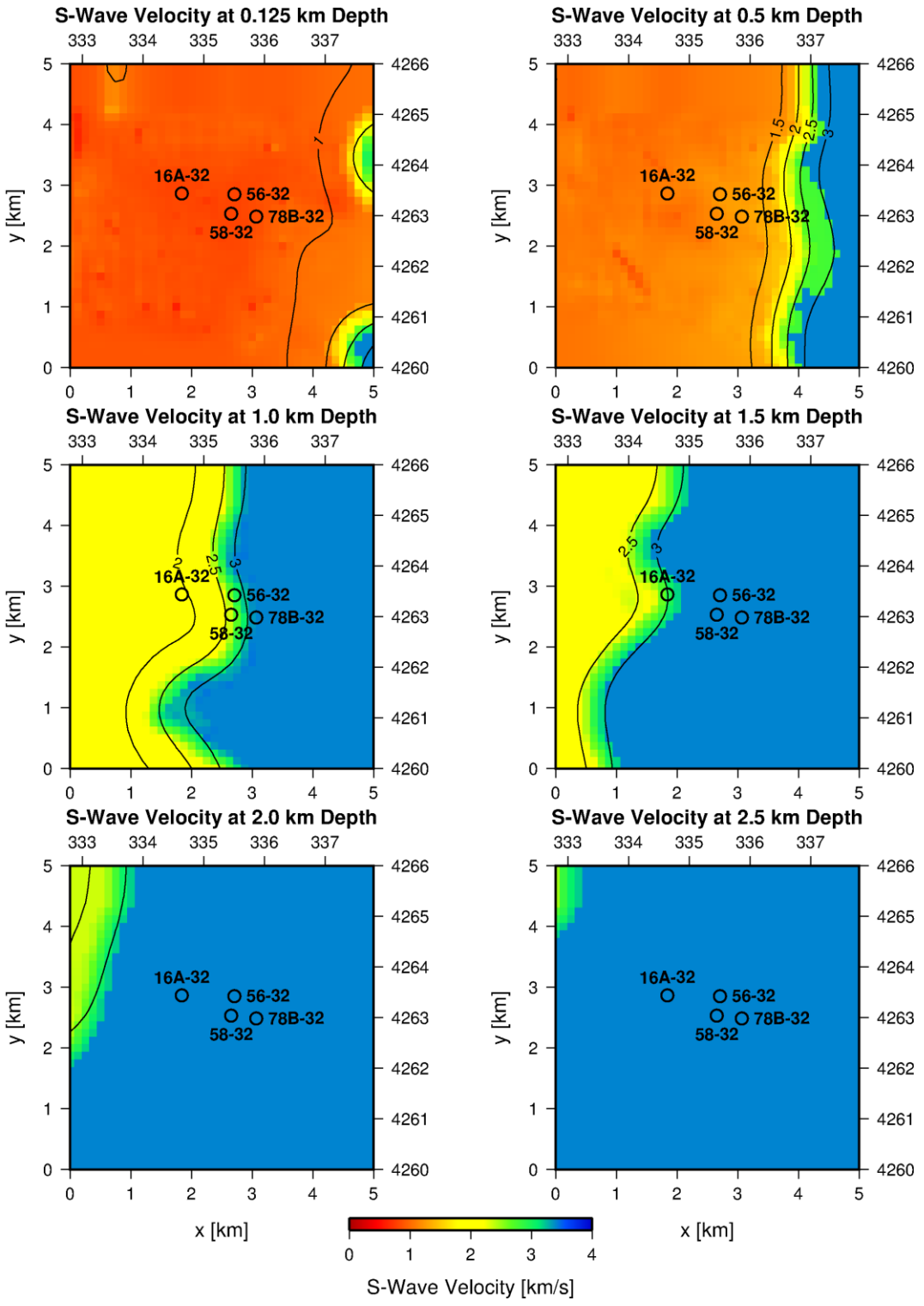

Figure 13. Horizontal sections through the 3D S-wave final velocity model. The depth is noted at the top of each panel. The locations of the wells are shown for reference.

3. Resolution Analysis of Seismic Wave Propagation in the Reservoir (Task 3.2)

The goal of Task 3.2 is to estimate the seismic resolution in the stimulated reservoir and to evaluate the potential for future seismic imaging campaigns to reliably image the generated fracture network. In the current analysis, we use the seismicity recorded during Stage III of the reservoir stimulation in well 16A-32 in April 2022, because the geometry of the stimulation experiment is similar to what is planned during the stimulation in well 16B-32. Therefore, the seismicity recorded during Stage III of the stimulation in April 2022 serves as a proxy for the data of the future stimulation experiment. The current task is divided into two parts, the first of which analyzes the resolution based on the seismic borehole sensors that were deployed during the April 2022 stimulation, while the second part analyzes all receivers that recorded the April 2022 stimulation including the surface-based nodal sensors and the DAS sensors that are scheduled to be deployed in well 16B-32 during the upcoming reservoir stimulation in Fall 2023.

3.1 Resolution Analysis with Borehole Sensors

The locations and trajectories of the injection well and the geophysical observation wells that were used during the April 2022 stimulation are presented in Figures 14 and 15. The injection well 16A-32 is vertical to 1,800 m depth, after which it deviates to the southeast until it reaches a final depth of 2,600 m. The geophysical observation wells are mainly vertical and reach depths between 1,000 m and 2,900 m. Twenty-one seismic sensors, indicated by the red crosses in Figures 14 and 15, were located in the observations wells within the granitic basement.

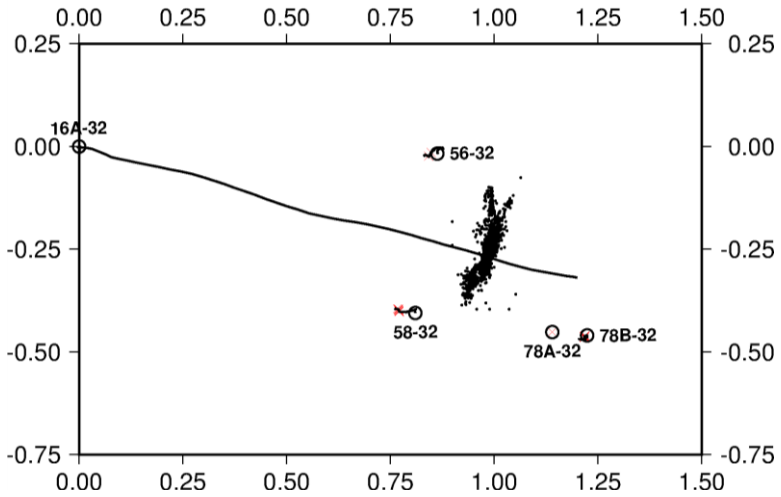

Figure 14. Map view with the locations and trajectories of the injection (16A-32) and geophysical observation wells (56-32, 58-32, 78A-32, 78B-32) at the FORGE site. The seismic sensors in each well are denoted by red crosses, while the seismicity recorded during Stage III of the April 2022 stimulation is given by the black dots.

The Stage III stimulation generated a seismic cloud of which 1,526 events were analyzed and located by Geo-Energie Suisse AG (GES) and which are shown by the black dots in Figures 14

and 15 (Pankow, 2022). The data analysis yielded 28,773 P- wave and 26,778 S-wave phase arrivals, which were subsequently used to estimate the seismic resolution in the stimulated volume.

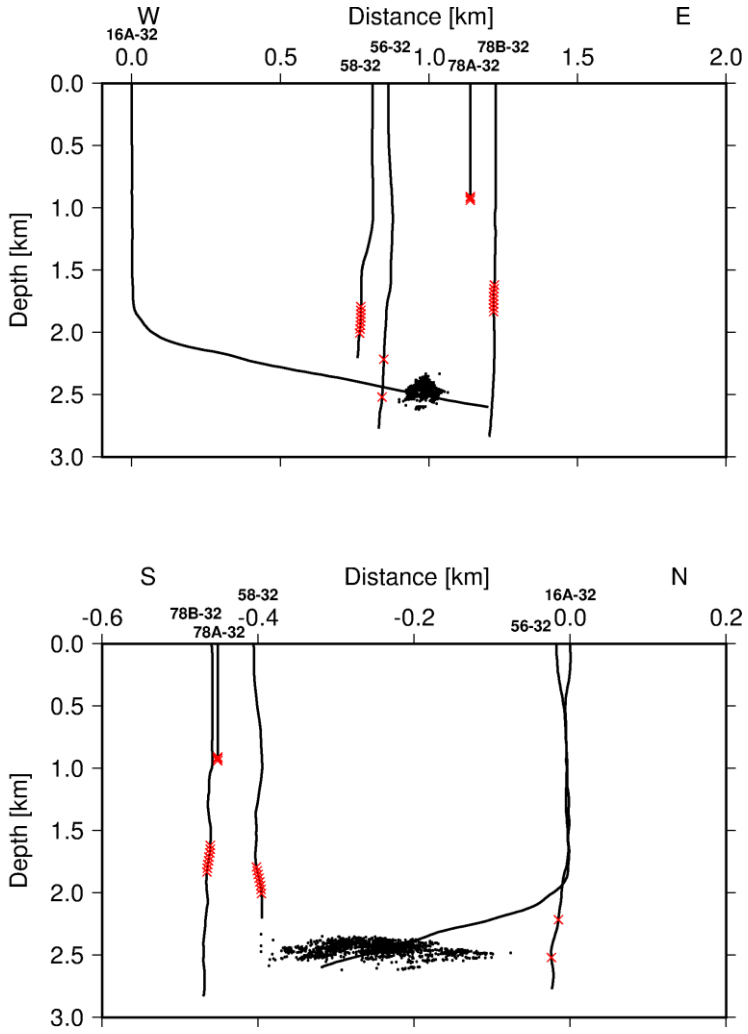

Figure 15. Vertical cross sections through the FORGE site with the geometry of the injection well 16A-32 and the geophysical observation wells 56-32, 58-32, 78A-32, and 78B-32. The seismic sensors in each well are denoted by red crosses. The seismicity recorded during Stage III of the April 2022 stimulation is given by the black dots.

For the resolution analysis, a homogeneous velocity model was assumed, because the seismic sensors were all located in the granitic basement, which is comprised of competent rock. The velocity values were the same as those used by GES for the analysis and location of the induced earthquakes (Vp = 5.83 km/s, Vs = 3.41 km/s). Using the earthquake hypocenters, the velocity model, and the sensor locations, seismic ray tracing was performed using the eikonal solver (Podvin and Lecomte, 1991) of the program tomoFDD (Zhang and Thurber, 2006, 2007; Gritto et al., 2013), which returned DWS values of the seismic velocities in the stimulated fracture volume. Gritto and Nihei (2019) showed that the normalized qualitative resolution estimates of DWS are

equivalent to quantitative resolution estimates based on singular value decomposition (Vasco, 2003). In seismic imaging it is generally accepted that a resolution of 0.1 is sufficient to reliably image the structure under investigation (i.e., Thurber et al., 2009; Lin et al., 2015). In the current task, we require a limit of DWS ≥ 0.2 to satisfy the threshold for resolution in the stimulated volume.

The results of the resolution analysis are presented in Figure 16, which shows a 3D view of the well geometries and seismicity at the FORGE site as well as the DWS of the P- and S-waves in the stimulated region. The seismic sensors are denoted by the gray cubes along the borehole trajectories, while the DWS is given by the colored cubic symbols. In the figures only values with a DWS ≥ 0.2 are plotted. It can be seen that the resolution is highest near the sensors, where the concentration of raypaths is densest. The resolution decreases with increasing distance from the sensors until it increases near the cloud of earthquakes again. In the stimulated volume, the resolution is equal or greater than the threshold of DWS ≥ 0.2. The P- and S-wave resolutions are nearly identical except for the sensors in borehole 78A-32. Due to the distance of the sensors in 78A-32 from the stimulated volume, the signal-to-noise amplitude ratio (S/R) is low such that no S-wave phase arrival times were estimated.

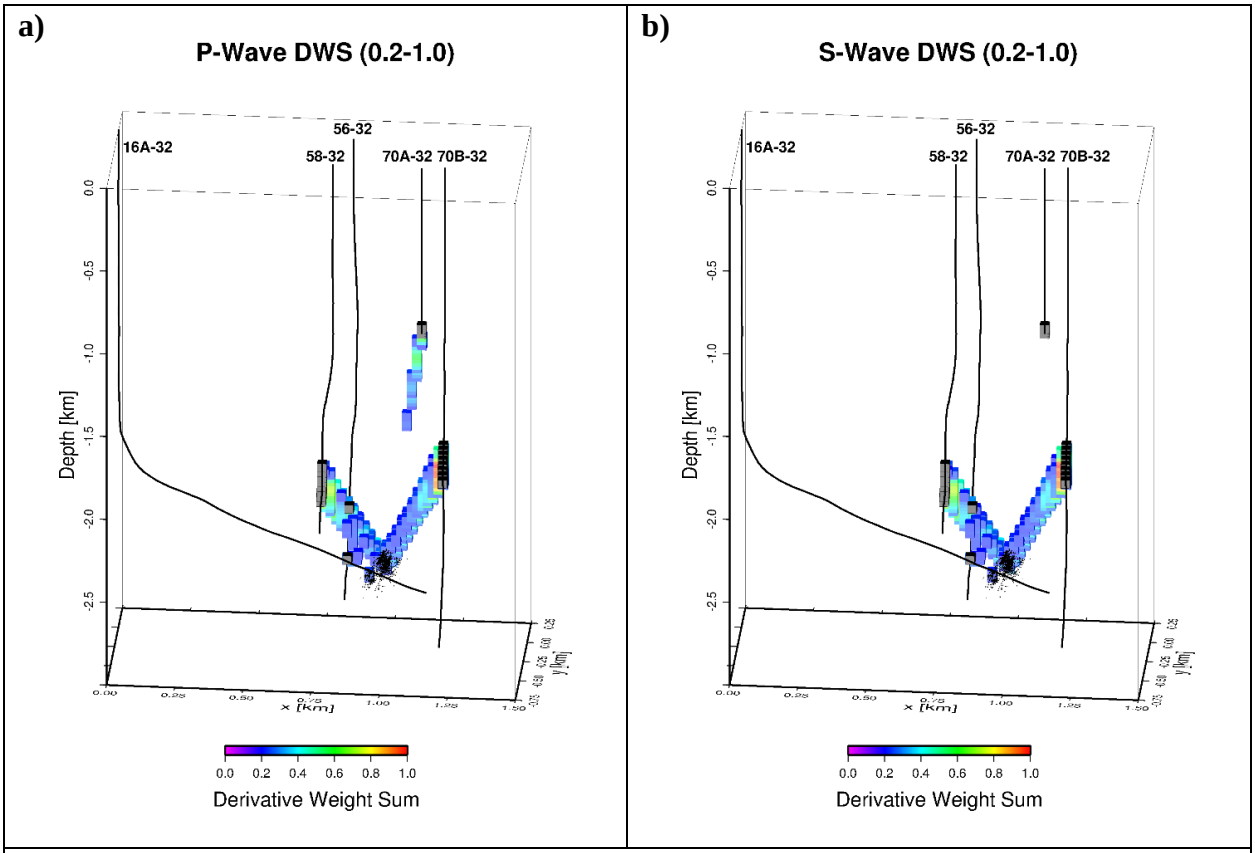

Figure 16. 3D view of the FORGE site displaying the trajectories of the injection and geophysical observation wells (black lines), the seismicity of the Stage III April 2022 stimulation (black dots), the seismic sensors (black cubes), and the DWS ≥ 0.2 for the **(a)** P-waves and (**b)** S-waves.

Figure 17 shows a similar 3D view, but for a plotting limit of DWS ≥ 0.5. At this higher threshold, the resolution is provided by the sensors in well 58-32, which are closest to the seismic cloud. It can be seen that some regions in the stimulated volume reveal DWS ≥ 0.5.

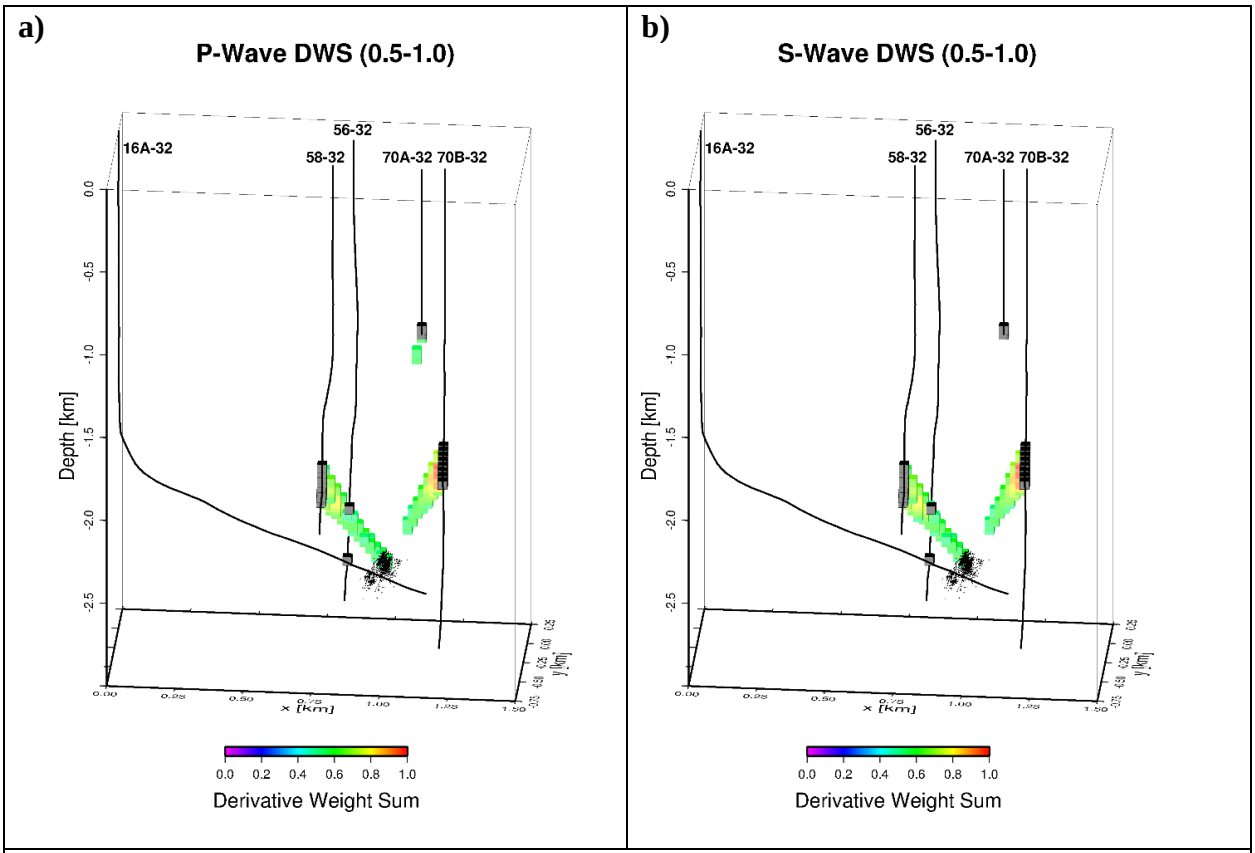

Figure 17. 3D view of the FORGE site displaying the trajectories of the injection and geophysical observation wells (black lines), the seismicity of the Stage III April 2022 stimulation (black dots), the seismic sensors (black cubes), and the DWS ≥ 0.5 for the **(a)** P-waves and (**b)** S-waves.

Similar results of the seismic resolution are presented in map view in Figure 18. The panels show horizontal sections through the FORGE area centered on the Stage III seismicity, with the surface locations of the observation boreholes and the trajectory of well 16A-32. The depth of the horizontal slices is denoted at the top of each panel. The seismicity in each panel, indicated by the black dots, represents projections of the earthquake hypocenters from 25 m above and below the depth of each panel. The first panel at 2300 m depth is located above the seismic cloud. Three resolution maxima are visible, which are associated with the P-waves propagating to the respective observation wells. As the depth of the panels increase into the seismic cloud, it can be seen that the maxima merge and the DWS level increases. The highest resolution (DWS ~ 0.5) is associated with the maximum seismic density at 2,400 m depth. As the panels dip below the seismic cloud the resolution quickly decays.

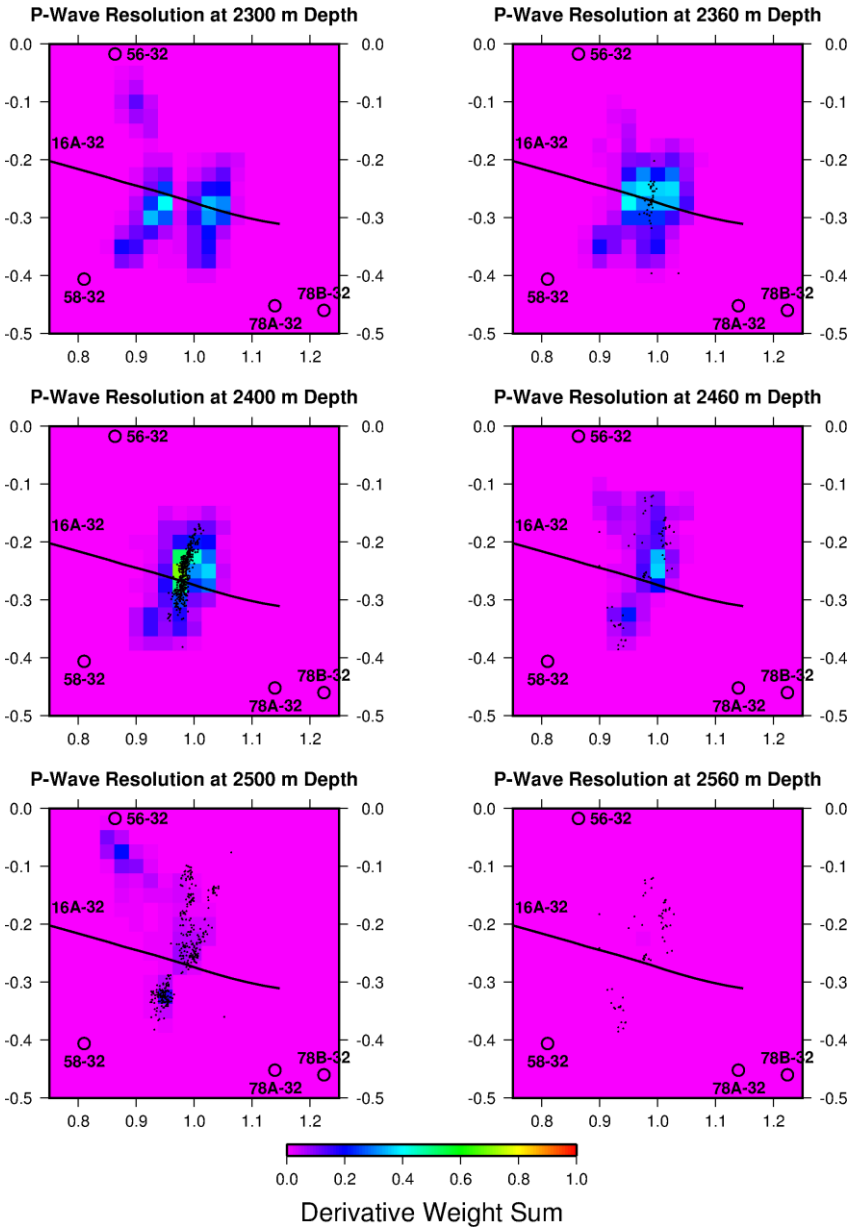

Figure 18. Map view of the P-wave DWS at different depth levels through the cloud of seismicity.

Similar results are observed in Figure 19 for the resolution of the S-waves. Maximum resolution of DWS ~ 0.5 are observed at 2,400 m depth. The results are comparable to the P-wave resolution, because the number of P- and S-wave phases, observed for the Stage III seismicity, is comparable.

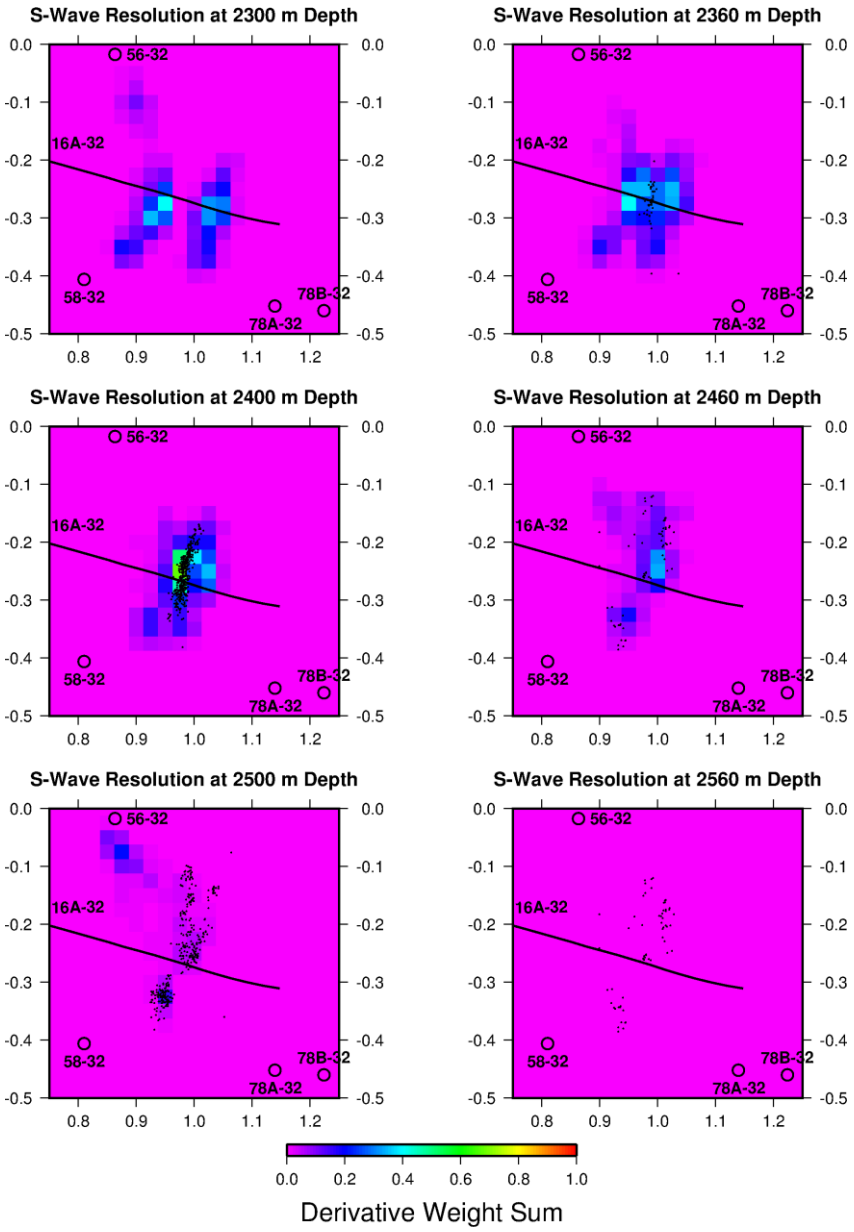

Figure 19. Map view of the S-wave DWS at different depth levels through the cloud of seismicity.

3.2 Resolution Analysis with Borehole, DAS, and Surface Sensors

The locations and trajectories of the injection well 16A-32, the future production well 16B-32, and the geophysical observation wells that were used during the April 2022 stimulation are presented in Figures 20 and 21. The trajectory of the future production well 16B-32 in this analysis is based on plans that are current as of the writing of this report but may be adjusted in the future. The

wellhead of 16B-32 is planned to be located about 38 m to the north-northwest of 16A-32, while the deviated section is located parallel and approximately 100 m above well 16A-32. Also shown in Figure 20 is an array with 13 pods of 16 nodal seismic sensors each, and a linear array of 70 nodal sensors, that were deployed along the surface, respectively, by the Univ. Utah and by Rice Univ., during the April 2022 stimulation. While the total number of nodal sensors by Rice Univ. amounted to 100, only the 70 sensors shown in Figure 20 were used for the current analysis, because the seismic data recorded by the first 30 sensors, located near the wellhead of 16A-32, were too noisy for data processing (Kim, 2023 personal communication). Additionally, the ambient noise and the long distance of the surface nodal sensors from the seismicity at depth, limited the analysis of the seismic data to events with magnitude M > -0.5 (Kim, 2023 personal communication; Murphy-Whidden, 2023, personal communication). This limited the number of events observed by the surface sensors to 126 out of 1,526 earthquakes detected and located by GES.

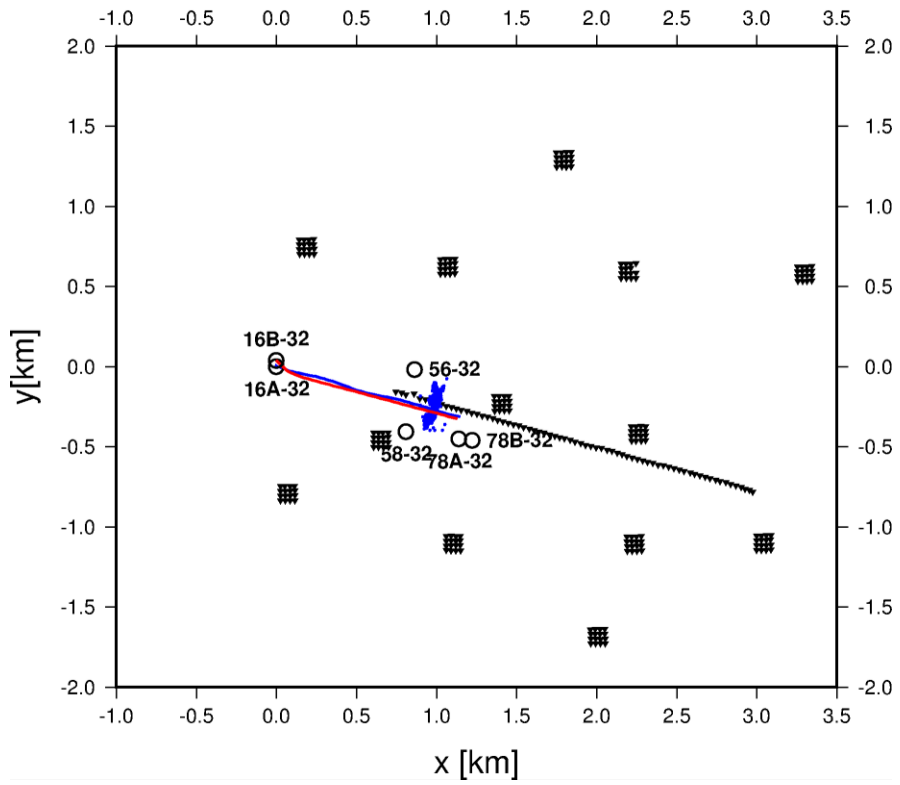

Figure 20. Map view with the locations and trajectories of the injection well 16A-32 (blue) and future production well 16B-32 (red), the geophysical observation wells (56-32, 58-32, 78A-32, 78B-32) and surface nodal sensors at the FORGE site. The seismicity recorded during Stage III of the April 2022 stimulation is given by the blue dots.

Two vertical cross sections through the FORGE site are presented in Figure 21, which displays the well trajectories and the earthquakes generated by the stimulation at ~ 2.5 km depth. The injection well 16A-32 and future production well 16B-32 are indicated, respectively, by the blue and red trajectories. The borehole sensors are denoted by the red crosses in the observation wells 56-32,

58-32, 78A-32, 78B-32, while the DAS sensors, modeled with a gauge length of 10 m are too dense to be distinguishable in the figure.

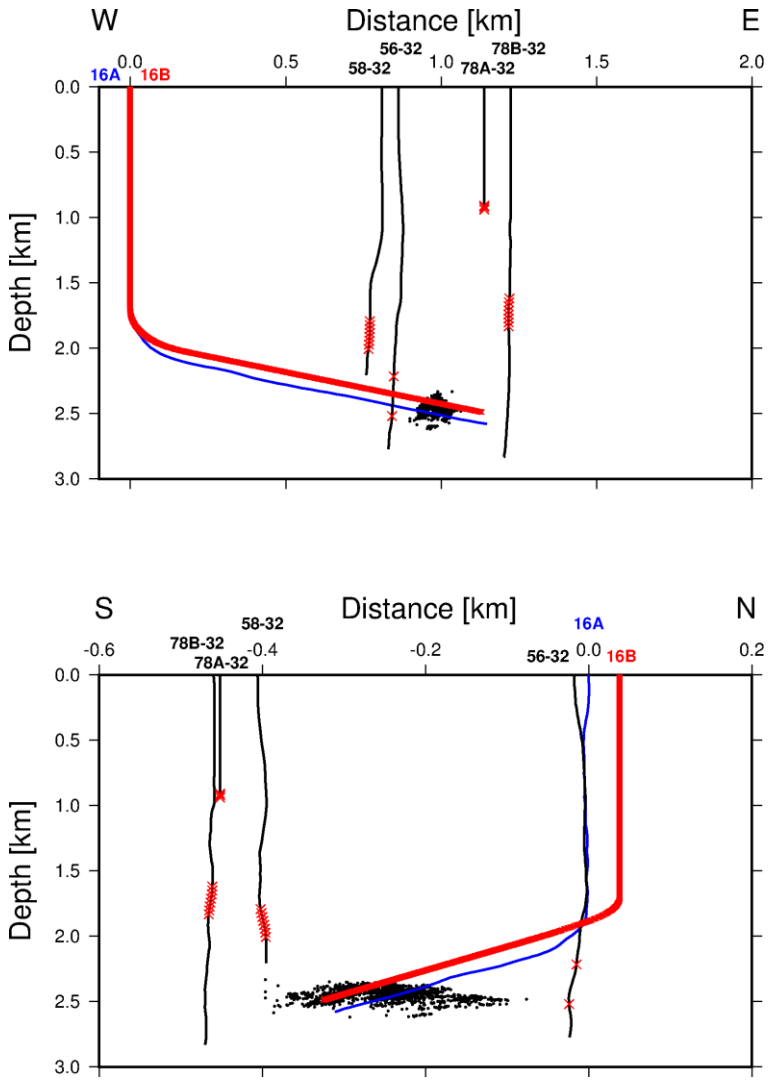

Figure 21. Vertical cross sections through the FORGE site with the geometry of the injection well 16A-32 (blue), the future production well 16B-32 (red), and the geophysical observation wells 56-32, 58-32, 78A-32, and 78B-32. The seismic sensors in the observation wells are denoted by red crosses. The DAS sensors in well 16B-32 with a gauge length of 10 m are too dense to be visually perceptible along the borehole trajectory. The seismicity recorded during Stage III of the April 2022 stimulation is given by the black dots.

For the resolution analysis with the sensors shown in Figures 20 and 21, the 3D velocity model developed in Task 3.1 was used. As mentioned above, the model accounts for the competent basement rock with constant P- and S-wave velocities (Vp = 5.83 km/s, Vs = 3.41 km/s), while the P-wave velocities in the sediments were derived by inverting the first arrival times of P-waves, and the S-wave velocities were obtained by scaling via a Vp/Vs ratio developed from DAS data

recorded in borehole 78A-32 (Lellouch et al., 2020). Similar to the case of the borehole sensors above, the DWS values were computed using the program tomoFDD by tracing seismic rays through the 3D velocity model from each event hypocenter to all borehole sensors, including the DAS sensors distributed in well 16B-32 at 10 m spacing. However, the seismic rays to the surface were limited to the 126 events of M -0.5 that were observed by surface seismic sensors.

The results of the resolution analysis are presented in Figure 22, which shows a 3D view of the well geometries and seismicity at the FORGE site, the locations of borehole and surface seismic nodal sensors, as well as the DWS of the P- and S-waves in the stimulated region. The seismic sensors are denoted by the gray cubes along the borehole trajectories and along the surface, while the DWS is given by the colored cubic symbols. The two eastern-most pods of seismic nodal sensors (for x > 3.0 km in Figure 20) are not shown to allow for a larger-scale plot. In the figure values with a threshold of DWS ≥ 0.01 are plotted, which represent the ray density to the various sensors in the model. At this threshold, no rays to the linear array of single nodal surface sensors are visible, while the pods of 16 sensors combined a sufficiently high number of rays to be displayed in this plot. However, most visible DWS values are below 0.05, which shields the view of the resolution in the cloud of seismic events.

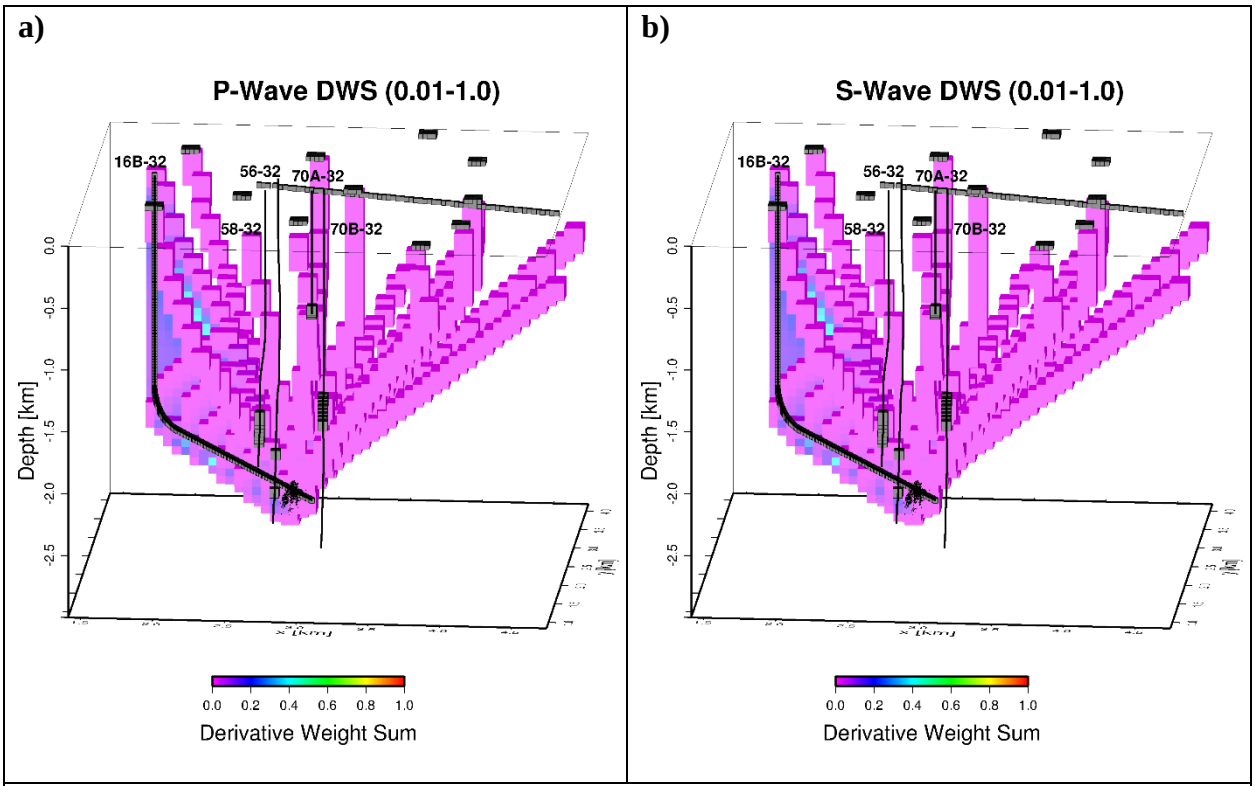

Figure 22. 3D view of the FORGE site displaying the trajectories of the injection and geophysical observation wells (black lines), the seismicity of the Stage III April 2022 stimulation (black dots), the seismic sensors (black cubes), and the DWS ≥ 0.01 for the **(a)** P-waves and (**b)** S-waves.

The view changes by raising the plotting threshold to DWS > 0.1, which is shown in Figure 23. At this level, the ray density is dominated by the wave propagation from the seismic events to the DAS sensors in well 16B-32. This is due to the modeled gauge length of 10 m, which results in a high-density of seismic sensors. At this level, DWS values up to 0.5 are visible along the ray paths to the DAS sensors. The best view of the resolution within the induced seismicity is given by a threshold of DWS > 0.5, which is shown in Figure 24. At this threshold, the DWS values are limited to the seismic cloud and to the seismic rays emanating from the cloud towards the DAS sensors in the bottom part of the well. At this threshold, DWS values in excess of 0.8 are visible within the seismic cloud.

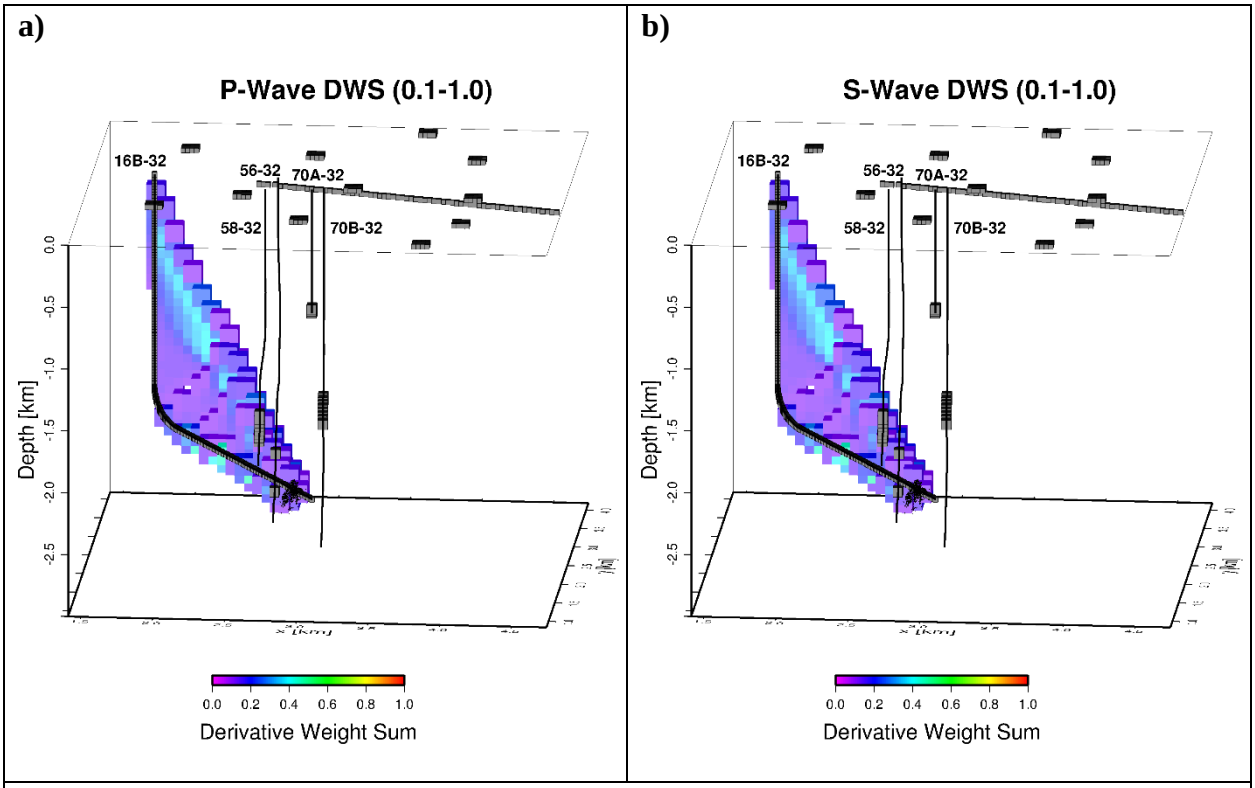

Figure 23. 3D view of the FORGE site displaying the trajectories of the injection and geophysical observation wells (black lines), the seismicity of the Stage III April 2022 stimulation (black dots), the seismic sensors (black cubes), and the DWS ≥ 0.1 for the **(a)** P-waves and (**b)** S-waves.

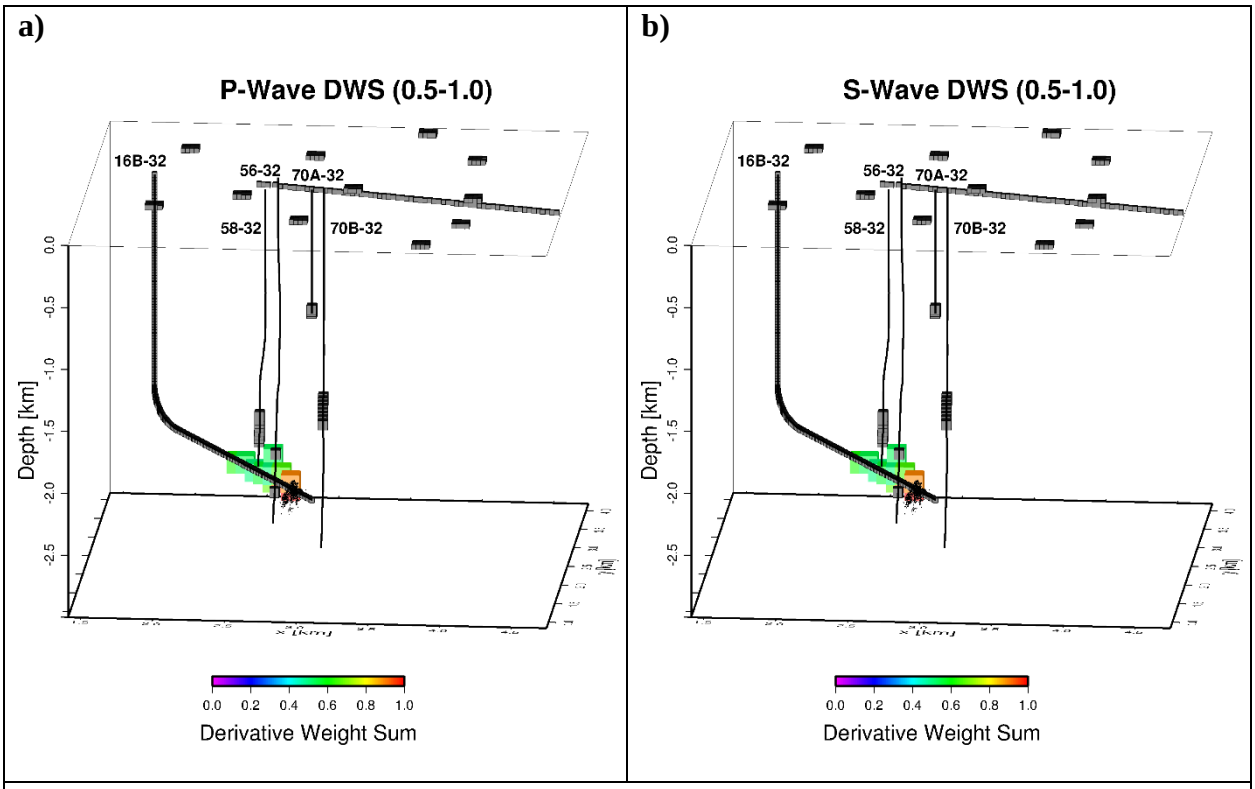

Figure 24. 3D view of the FORGE site displaying the trajectories of the injection and geophysical observation wells (black lines), the seismicity of the Stage III April 2022 stimulation (black dots), the seismic sensors (black cubes), and the DWS ≥ 0.5 for the **(a)** P-waves and (**b)** S-waves.

The DWS results in map view are presented in Figure 25 and 26, for the P- and S-wave resolution, respectively. The panels show horizontal sections through the FORGE area centered on the Stage III seismicity. The figures show a zoomed view of the activated fracture volume, to provide a better perspective of the resolution in the area of interest. Therefore, only the vertical observation wells, the bottom of well 16B-32, and some of the surface nodal sensors are visible. The depth of the horizontal slices is denoted at the top of each panel, while the seismicity in each panel, indicated by the black dots, represents projections of the earthquake hypocenters from 30 m above and below the depth of each panel. The first panel at 2,300 m depth is located above the seismic cloud. An elongated DWS maximum with values between 0.2 – 0.6 is visible extending from the center towards the west. This maximum is associated with P-waves propagating from the seismic could to the DAS sensors in the bottom part of well 16B-32. As the depth increases to 2,370 m it reaches the top of the seismic cloud and the DWS values increase above 0.8 in this section of the stimulated volume. The panel at 2,430 m slices through the center of the seismic could, which results in the highest observed resolution values of DWS > 0.9. As the depth decreases to the lower half of the seismic cloud (2,500 m) the maximum DWS values drop to 0.3 Below this depth the resolution quickly decays to values below DWS < 0.1.

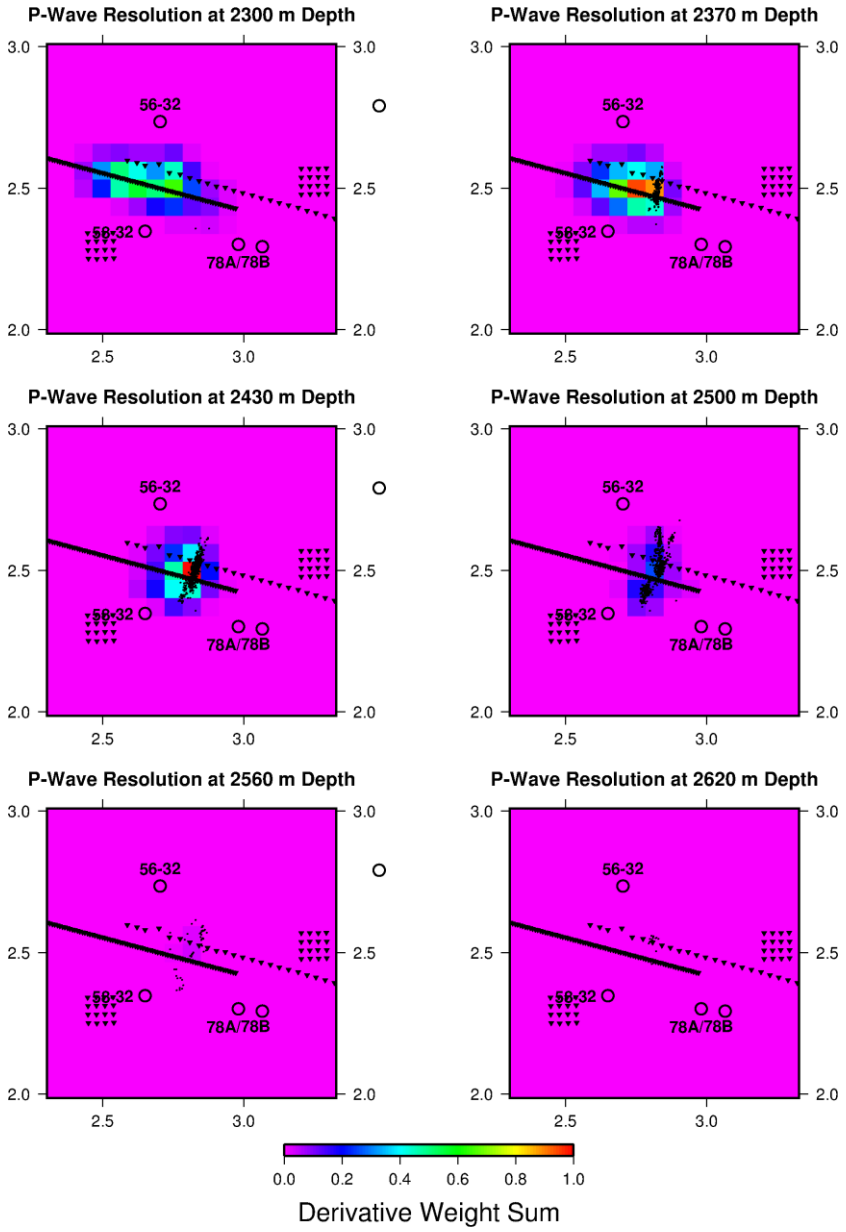

Figure 25. Map view of the P-wave DWS at different depth levels through the cloud of seismicity. The surface locations of the vertical observation wells (open circles), the surface nodal seismic sensors (inverted triangles), as well as the trajectory of the bottom section of well 16B-32 are projected onto each panel.

Similar results are observed in Figure 26 for the resolution of the S-waves. Because the number of observed S-waves in the seismic borehole sensors in wells 56-32, 58-32, 70A-32, and 70B-32 was similar to that of the P-waves (Pankow, 2022), and because the unavailability of surface seismic nodal data for the current task, and for the yet to be deployed DAS sensors, the number of the

observed P- and S-waves in the latter sensors was kept equal. Consequently, the maximum resolution of DWS > 0.9 are observed at 2,430 m depth.

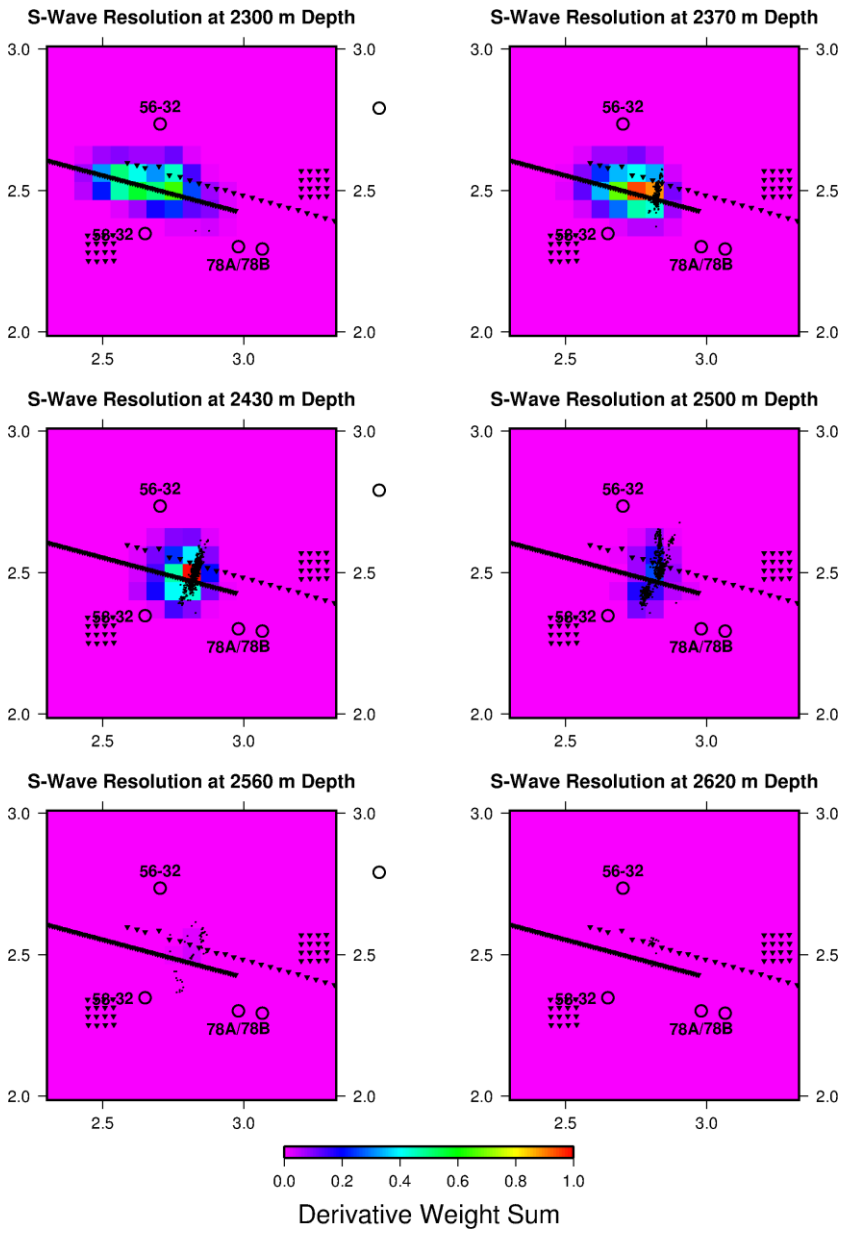

Figure 26. Map view of the S-wave DWS at different depth levels through the cloud of seismicity. The surface locations of the vertical observation wells (open circles), the surface nodal seismic sensors (inverted triangles), as well as the trajectory of the bottom section of well 16B-32 are projected onto each panel.

4. Conclusions

A 3D velocity model for the larger FORGE area was developed using RMS velocities of the seismic reflection survey and seismic velocity logs from borehole measurements as an input model. To improve the accuracy of the model in the shallow subsurface, travel times phase arrivals of the direct propagating P-waves were determined from the seismic reflection data, using PhaseNet, a deep-neural-network-based seismic arrival time picking method, which resulted in more than 1,200,000 P-wave travel times. In a first step, a subset of the travel times were inverted to derive a preliminary 3D velocity model. The results showed that the input velocity model needed improvement as the resulting model appeared too fast in the easter region of the FORGE area. Therefore, the velocities of the input model were scaled down in the sediments and a constant basement velocity of 5.83 km/s was chosen, which improved the match between the theoretically computed and observed P-wave travel times. In a subsequent step, 1,200,000 P-wave travel times were inverted to obtain the final 3D P-wave velocity model. To map the P-wave velocities to S-wave velocities, a Vp/Vs ratio profile was derived using the results of a DAS experiment in borehole 78A-32. The resulting P- and S-wave velocity models reveal low velocities in the shallow sediments, which gradually increase towards the sedimentary/basement interface. Horizontal sections through the velocity models indicate that the contact between the sediments and the basement is not planar at intermediate depth (1.0 km, 1.5 km).

The results of seismic resolution in the fractured reservoir generated during the Stage III stimulation in April 2022 illustrate that the DWS of the P- and S-waves is sufficiently high to perform reliable seismic imaging based on the borehole seismic sensors alone. The DWS was found to range from 0.2 - 0.5 throughout the cloud of seismic events in the stimulated region of the reservoir, which is higher than the generally accepted imaging threshold of 0.1.

Modeling the seismic resolution for the future stimulation in well 16B-32 the geometry of the induced seismic events during the stimulation in April 2022 was utilized. The modeling also employed the geometry of the seismic borehole and nodal surface seismic sensors used during the stimulation in April 2022, as well as the trajectory of the future well 16B-32 with DAS sensors distributed at 10 m gauge length. Additionally, it was assumed that P-and S-waves are detectable at each DAS sensor, which represents the best-case scenario. However, the sensitivity of the DAS cable within the deviated section of well 16B-32 pointing towards the cloud of induced seismicity increases the chances of recording seismic data with good signal-to-noise amplitude ratio. Additionally, the number of observed P- and S-waves at the surface were kept in accordance with what was observed during the April 2022 stimulation. The modeling revealed the potential for high seismic resolution in the stimulated fracture volume. While the surface seismic data did not contribute noticeably to the resolution the addition of the DAS sensors, with their high spatial density, increases the resolution considerably compared to the case of seismic borehole sensors in the vertical observation wells only (first part of Task 3.2). However, even if seismic DAS data were unavailable, the modeling of seismic borehole sensors in the first part of Task 3.2, showed sufficient resolution (DWS 0.2 – 0.5) to perform reliable seismic imaging in the future stimulated reservoir.

5. References

Gritto, R., S.H. Yoo and S.P. Jarpe, 2013. Three-dimensional seismic tomography at The Geysers geothermal field, CA, USA, *Proceedings, 38th Workshop Geothermal Reservoir Engineering*, SGP-TR-198.

Gritto, R. and K.T. Nihei, 2019. High-Resolution Imaging of Geothermal Flow Paths Using a Cost-Effective Dense Seismic Network, Task 2: Dense Network Design, *Final Report*, California Energy Commission, EPC-16-021, pp. 1-21.

Gritto, R. and D.W. Vasco, C. Chan, 2023. Development of a Reservoir Seismic Velocity Model, *Task 3 Milestone Report 3.1*, LBNL FORGE Project 3-2535, 1-15, https://gdr.openei.org/submissions/1470.

Lellouch, A., N.J. Lindsey, W.L. Ellsworth, and B.L. Biondi, 2020. Comparison between Distributed Acoustic Sensing and Geophones: Downhole Microseismic Monitoring of the FORGE Geothermal Experiment, *Seismol. Res. Lett*., **91**, 3256–3268, doi: 10.1785/0220200149.

Lin, G., P. M. Shearer, F. Amelung, and P. G. Okubo, 2015. Seismic tomography of compressional wave attenuation structure for Kilauea Volcano, Hawai'i, *J. Geophys. Res*. Solid Earth, **120**, 2510–2524, doi:10.1002/2014JB011594.

Miller, J., 2019. Utah FORGE: Seismic Reflection Data. United States. https://dx.doi.org/ 10.15121/1542059.

Pankow, K., 2022. Seismic Data from the Well 16A-32 Stimulation April, 2022. United States. https://dx.doi.org/10.15121/1879450.

Podvin, P., and I. Lecomte, 1991. Finite difference computation of travel times in very contrasted velocity models: A massively parallel approach and its associated tools, *Geophys. J. Int.*, **105**, 271–284.

Thurber, C. H., and D. Eberhart-Phillips, 1999. Local earthquake tomography with flexible gridding, *Comp. and Geosci*., **25**, 809–818.

Thurber, C., H. Zhang, T. Brocher, and V. Langenheim, 2009. Regional three-dimensional seismic velocity model of the crust and uppermost mantle of northern California, *J. Geophys. Res*., **114**, B01304, doi:10.1029/2008JB005766.

Vasco, D. W., L.R. Johnson and O. Marques, 2003. Resolution, uncertainty, and whole Earth tomography, J. Geophys. Res., 18, 2022, doi:10.1029/2001JB000412.

Zhang, H., and C. Thurber, 2007. Estimating the model resolution matrix for large seismic tomography problems based on Lanczos bidiagonalization with partial reorthogonalization, *Geophys. J. Int*., **170**, 337– 345.

Zhang, H. and C. H. Thurber, 2006. Development and Applications of Double-difference Seismic Tomography, *Pure Appl. Geophys*., **163**, DOI 10.1007/s00024-005-0021-y, 373-403.

Zhu W. and G. C. Beroza, 2019. PhaseNet: a deep-neural-network-based seismic arrival-time picking method, *Geophys. J. Int*., **216**, 261–273, doi: 10.1093/gji/ggy423.